Journal of
Applied
Crystallography
ISSN 1600-5767

Received 25 July 2014
Accepted 15 October 2014

Synthesis and nucleation studies on L-leucine hydrobromide: a promising nonlinear optical material

Radha Rani,[a,b] Kanika Thukral,[a,c] Anuj Krishna,[a,c] Geetanjali Sharma,[a] Narayanasamy Vijayan,[a] Brijesh Rathi[d] and Godavarthi Bhagavannarayana[a]*

[a]Crystal Growth and X-ray Analysis Activity, CSIR–National Physical Laboratory, Dr K. S. Krishnan Marg, New Delhi 110 012, India, [b]ISERC, Visva Bharati University, Shantiniketan 731235, India, [c]Academy of Scientific and Innovative Research, CSIR–National Physical Laboratory, New Delhi 110 012, India, and [d]Department of Chemistry, Sri Venkateswara College, University of Delhi, New Delhi 110021, India. Correspondence e-mail: bhagavan@nplindia.org

To achieve good quality bulk size crystal growth, an assessment of the nucleation kinetics of a semi-organic L-leucine hydrobromide (L-LHBr) crystal was carried out using double-distilled water as solvent medium. The effect on metastable zone width (MSZW) with increasing temperature and on induction period with varied supersaturation level was determined experimentally and was found to be very well in accordance with the nucleation theory prospects. Thereafter, various other nucleation parameters, such as Gibbs free energy and interfacial energy, were also determined. The knowledge of these nucleation parameters indicated the requisite temperature domain and the appropriate growth technique, leading to the successful single-crystal growth of L-LHBr by slow cooling in the temperature range 298–291 K. The cooling rate of 0.25 K per day was optimized after repeated trials. X-ray diffraction and Raman analysis were performed on grown crystals for the verification of the material. High-resolution X-ray diffraction analysis was used to assess the crystalline perfection of the grown crystals. To further explore the properties of the grown crystals, photoluminescence and time decay studies, etching analysis, and *Z*-scan measurements were performed.

1. Introduction

Advances in research and technology in various fields are highly dependent on crystals. Crystals displaying favourable piezoelectric, ferroelectric and nonlinear properties are in great demand, on account of their suitability for many applications (Senthil Pandian *et al.*, 2012; Rani *et al.*, 2013; Shkir *et al.*, 2013). Consequently, much work on the growth of bulk single crystals is being concentrated on detecting the feasibility and workability of crystals for device fabrication. The fitness of crystals for such applications is in turn related to the optimization of the growth process by studies on the nucleation kinetics. Once the needed supersaturation level is achieved, nucleation is the driving force for crystallization in the growth of crystals from solution growth methods. L-Leucine hydrobromide, L-LHBr ($C_6H_{14}NO_2^+\cdot Br^-$), is a semi-organic nonlinear optical material with a second harmonic generation efficiency reported to be four times that of potassium dihydrogen phosphate (KDP) (Adhikari & Kar, 2013). L-LHBr belongs to space group $P2_12_12_1$ with an orthorhombic lattice family (Adhikari & Kar, 2013; Subramanian, 1967). The growth of the L-LHBr crystal is influenced by a change in pH of the KDP mother solution (Adhikari & Kar, 2013). As reported by Subramanian (1967), L-LHBr crystals grown by slow evaporation are thin and soft and quickly disappear in ambient conditions because of their hygroscopic nature. Therefore, there is a need for a thorough study of the nucleation and growth parameters needed to grow bulk size crystals. In the present investigation, a detailed analysis of the nucleation kinetics including induction period and metastable zone width was carried out. This study enables us to grow reasonably good quality bulk size single crystals. The structure and functional groups were identified by powder X-ray diffraction (XRD) and Fourier transform (FT)–Raman studies. The crystalline perfection was assessed by high-resolution XRD and etching techniques. Photoluminescence (PL) and time-resolved photoluminescence (TRPL) studies were carried out to assess the optical quality of the crystal. Third-order nonlinear properties were also assessed by the *Z*-scan technique.

2. Experimental

2.1. Solvent selection and solubility measurements

The selection of an appropriate solvent is of prior concern in the growth of bulk crystals from the solution growth

method, as the solvent is directly responsible for the yield. This relation between a solute and solvent system is basically governed by the solubility of the solute in the corresponding solvent. Solvent and solubility factors (such as temperature and pressure) are important elements in the attainment of supersaturation, which induces the nucleation process. To determine the solubility, experiments were performed using a constant volume of 50 ml of the solution in an airtight container with constant magnetic stirring for 5–6 h at a particular temperature, in order to achieve homogeneity of the solution. The experiments were carried out in a constant temperature bath (CTB) having a stability of ±0.01 K, with sustained circulation of water in the CTB for consistency at the set temperature. The solubility of the compound L-LHBr was determined gravimetrically in water for different temperatures (293, 298, 303, 308 and 313 K) at a pH value of 0.88. The results are shown in Fig. 1, demonstrating the solubility curve. The optimal pH value for the growth of L-LHBr crystals was assessed by growing the crystals at different pH values, and it was found that comparatively good quality crystals were obtained at the pH value of 0.88. This is in very good agreement with the reported literature (Adhikari & Kar, 2013). The growth process in the present investigation was further assessed through a nucleation kinetics study, with the aim of improving the grown crystals. L-LHBr salt was synthesized by reacting L-leucine and hydrobromic acid, which were taken in stoichiometric proportions. The purity of the synthesized material was further improved through the process of recrystallization.

2.2. Metastable zone width and induction period measurements

In a homogeneous solution and at a particular temperature, the solute remains in the solvent until a sufficiently high level of supersaturation is reached that spontaneous nucleation can be achieved. This correspondence between supersaturation and the spontaneous onset of crystallization is quantified by the metastable zone width (MSZW), as shown in Fig. 2. The MSZW basically signifies the stability of the system in a particular temperature regime. The higher the MSZW, the more suitable the conditions for crystal growth. Induction period is yet another important parameter to focus on. Since there is very little time lag between the attainment of supersaturation and the visibility of the first speck of the crystalline particle (commonly referred to as the critical nucleus), the induction period is identified with the detection of the first critical nuclei. The calculation of the MSZW and the induction period is done in accordance with the polythermal method (Nielsen, 1964).

To obtain the MSZW, the saturated mother solution prepared at a specified temperature is cooled at a constant rate. Then the temperature at which the first nucleation occurred is recorded. The difference between the temperature at which the saturated solution is prepared and the nucleation temperature obtained gives the MSZW. Knowledge of the MSZW renders valuable information about the growth prospects, the temperature regime and the accessible supersaturation levels in which the crystallization process is optimized for a particular solute–solvent system. Saturation solutions were prepared at different temperatures (293, 298, 303, 308 and 313 K), and the corresponding nucleation temperatures were measured as demonstrated in Fig. 2. As seen in the figure, one can find a larger MSZW at lower

Table 1
Solubility, nucleation temperature, induction period and metastable zone width of L-LHBr.

Serial number	Saturation temperature (K)	Solubility (g per 100 ml) (C*)	Nucleation temperature (K)	Induction period (τ) (in min)	Metastable zone width
1	293	36.19	287.17	15.44	5.83
2	298	38.92	294.94	12.25	3.06
3	303	42.27	301.04	8.13	1.96
4	308	54.54	306.86	3.36	1.14
5	313	74.87	312.26	1.28	0.74

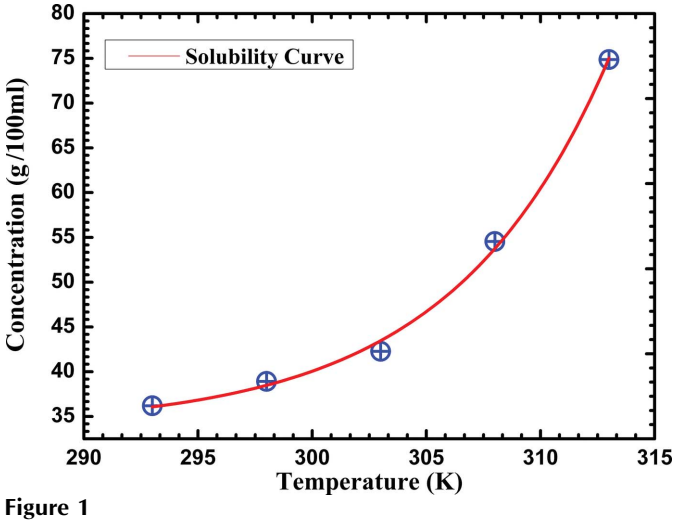

Figure 1
Solubility curve of L-LHBr.

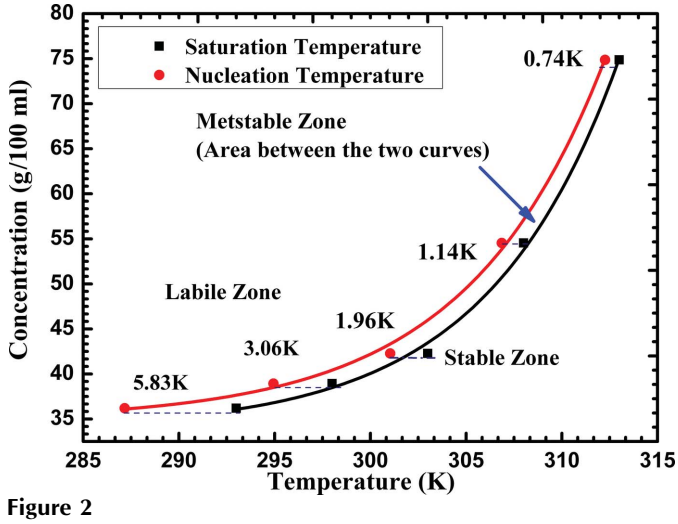

Figure 2
Metastable zone width of L-LBBr.

temperatures. The induction period (τ) at different supersaturation levels was also determined. Table 1 reports the solubility, nucleation temperature, induction period and MSZW recorded at the different saturation temperatures.

2.3. Nucleation kinetics

2.3.1. Theory. The detailed assessment of a solute–solvent system can be implemented by evaluation of several parameters comprising what is known as nucleation kinetics. Nucleation theories by Nielsen, Beckers and Doring (Nielsen, 1964; Yang *et al.*, 2010) have established the fact that the formation of a small embryonic cluster (after attainment of the critical size) triggers a macroscopic phase transformation in the case of homogeneous nucleation. Precisely, the change in Gibbs free energy between the spherical crystalline nuclei formed and the neighbouring mother solution is given by (Yang *et al.*, 2010; Selvaraju *et al.*, 2006; Kanagasekaran *et al.*, 2007)

$$\Delta G = \tfrac{4}{3}\pi r^3 \Delta G_{\rm V} + 4\pi r^2 \sigma. \quad (1)$$

Here $\Delta G_{\rm V}$ accounts for the energy change per unit volume, σ accounts for the interfacial energy of the solid nuclei relative to the solution, a critical parameter for formation of nuclei, and r is the radius of the nuclei formed. The classical theory of nucleation suggests that the volume excess free energy can be calculated as

$$\Delta G_{\rm V} = -\frac{kT \ln S}{V}, \quad (2)$$

where V is the molecular volume and k is the Boltzmann constant. The interfacial energy can be calculated through the experimentally obtained induction period τ at a particular saturation temperature T and supersaturation ratio S:

$$\ln \tau = \ln B + \frac{16\pi\sigma^3 V^2}{3k^3 T^3 (\ln S)^2}. \quad (3)$$

The constant B is found to depend weakly on the temperature. Thus, the interfacial energy is calculated directly from the slope as per the following equation:

$$m = \frac{16\pi\sigma^3 V^2}{3k^3 T^3}. \quad (4)$$

Consequently, the interfacial energy is

$$\sigma = kT\left(\frac{3m}{16\pi V^2}\right)^{1/3}. \quad (5)$$

The critical stage accounts for the formation of the critical particle, and at that point the change in free energy is

$$\frac{{\rm d}(\Delta G)}{{\rm d}r} = 0. \quad (6)$$

The radius of the critical nucleus thus obtained is

$$r^* = \frac{-2\sigma}{\Delta G_{\rm V}} \quad (7)$$

and the associated critical free energy

Table 2
Nucleation kinetics parameters calculated for L-LHBr.

Saturation temperature (K)	$S = C/C^*$	σ (mJ m^{-2})	$\Delta G_{\rm V}$ (J m^{-3}) (10^6)	ΔG^* (10^{-21})	r^* (nm)
293	1.1	1.55	−1.55	25.75	19.93
	1.2	1.33	−2.97	4.41	8.91
	1.3	1.11	−4.28	1.28	5.23
	1.4	0.93	−5.48	0.45	3.39
298	1.1	1.57	−1.58	26.19	19.93
	1.2	1.35	−3.02	4.49	8.91
	1.3	1.14	−4.35	1.31	5.23
	1.4	0.95	−5.57	0.46	3.39
303	1.1	1.60	−1.60	26.63	19.93
	1.2	1.37	−3.07	4.57	8.91
	1.3	1.16	−4.42	1.33	5.23
	1.4	0.96	−5.67	0.46	3.39
308	1.1	1.63	−1.63	27.07	19.93
	1.2	1.39	−3.12	4.64	8.91
	1.3	1.17	−4.50	1.35	5.23
	1.4	0.97	−5.77	0.47	3.39
313	1.1	1.65	−1.66	27.52	19.93
	1.2	1.41	−3.17	4.72	8.91
	1.3	1.19	−4.57	1.38	5.23
	1.4	0.99	−5.85	0.48	3.39

$$\Delta G^* = \frac{16\pi\sigma^3}{3\Delta G_{\rm V}^2}. \quad (8)$$

2.3.2. Theoretical estimation of interfacial energy. The following relation given by Teychené & Biscans (2008) is used for the direct theoretical calculation of the interfacial energy, paving the way for correlation of the theoretical and experimental results:

$$\sigma = 0.25kTV^{-2/3}(0.7 - \ln x_{\rm m}). \quad (9)$$

Here $x_{\rm m}$ is the mole fraction of the solute.

Using these equations, the values of the volume excess free energy, interfacial energy, radius of the critical nucleus and critical free energy were calculated for different temperature and supersaturation ratios. The results are collected in Table 2.

2.4. Crystal growth

The solubility measurements and MSZW of L-LHBr indicated the way to grow large size single crystals through the slow cooling technique. As described in §2.2, crystal growth was carried out with the initial saturated solution made at 298 K by lowering the temperature to 291 K. Several trials with different cooling rates were attempted, and it was found that a good size single crystal (16 × 4 × 3 mm) of L-LHBr with optical quality could grow with a temperature lowering rate of 0.25 K per day. One may realize that in the course of the growth process, which was started at 25 K, the concentration of the solution decreases with time during cooling (as some fraction of the solute becomes part of the growing crystal). Hence, even when we reach the considerably lower temperature of 18 K, the saturation condition remains in the metastable zone. Fig. 3(*a*) shows an L-LHBr crystal (16 × 4 ×

3 mm) grown through the conventional slow evaporation solution technique (SEST), and Fig. 3(*b*) shows a crystal grown by the slow cooling method after the optimization of growth parameters. The optically good quality crystals grown through the slow cooling method were put forward for further characterization in order to explore the sample properties.

3. Results and discussion

3.1. Crystallization kinetics

In the present investigation, the variations in induction period with different supersaturation ratios and temperatures were recorded as shown in Fig. 4. The figure clearly shows that as the supersaturation ratio increases there is a decrease in the induction period, affirming that nucleation rate increases with increasing supersaturation ratio. Also, there is a gradual decrease in induction period with increasing temperature, possibly because of the enhancement in the nucleation rate. In this graph the points represent the experimentally obtained values and the straight line is the linear fit to it. Fig. 5 shows the $\ln\tau$ *versus* $1/(\ln S)^2$ plot. For more efficient determination of experimentally obtained interfacial energy, the points were taken from the linearly fitted plots of induction period *versus* supersaturation ratio. As seen in the figure, the plots do not follow a straight line over the entire measured range of *S*. As per equation (4), this graph is supposed to be a straight line. A similar deviation from straight line behaviour has also been observed for many crystals in the literature (Kanagasekaran *et al.*, 2007; Kandasamy *et al.*, 2008). This shows that the value of *B* is not strictly constant and depends on the temperature and the value of *S*. So, to obtain the slope we have chosen an intermediate point at $S = 1.2$ for the curves with saturation temperatures 293 and 298 K and calculated the interfacial energy values accordingly through equation (4). For the corresponding theoretical calculations [through equation (9)], the value of x_m (= *S*) was also taken as 1.2. For the curve with saturation temperature of 303 K, a convenient intermediate value of 1.07 for *S* was chosen to determine the slope of the curve, because of the lack of experimental values above 1.2, and the same value of x_m was used to calculate the theoretical interfacial energy. Table 3 gives the values of the slope,

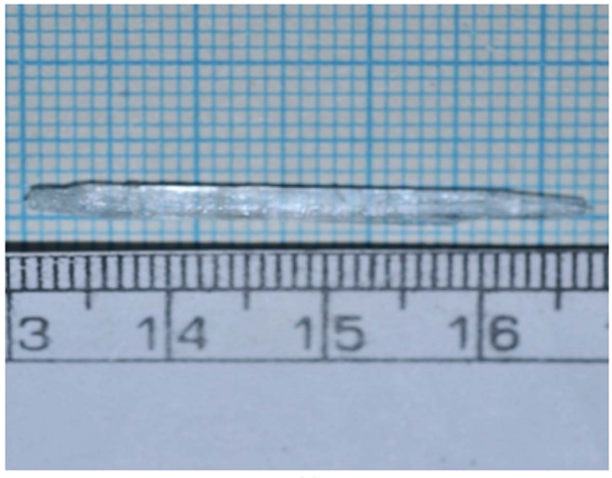

(*a*)

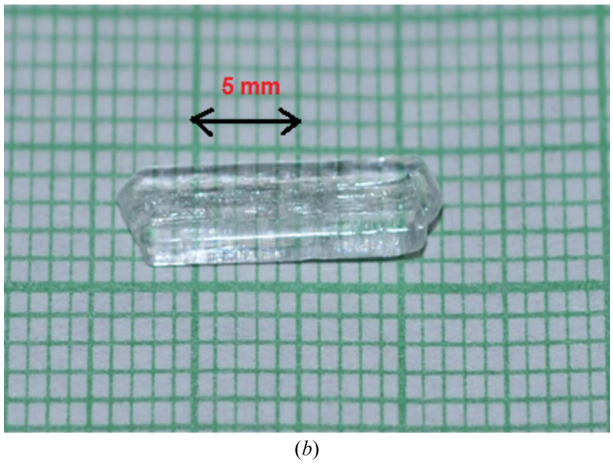

(*b*)

Figure 3
(*a*) L-LHBr crystal grown through SEST. (*b*) L-LHBr crystal grown after optimization of parameters.

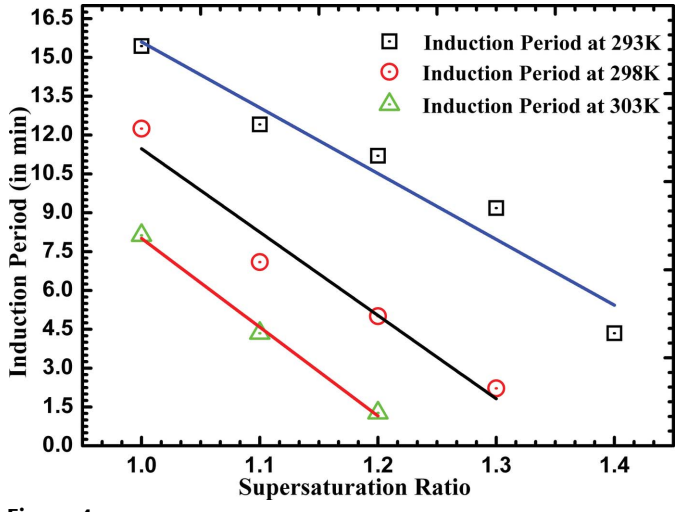

Figure 4
Variation of induction period with supersaturation ratio of L-LHBr.

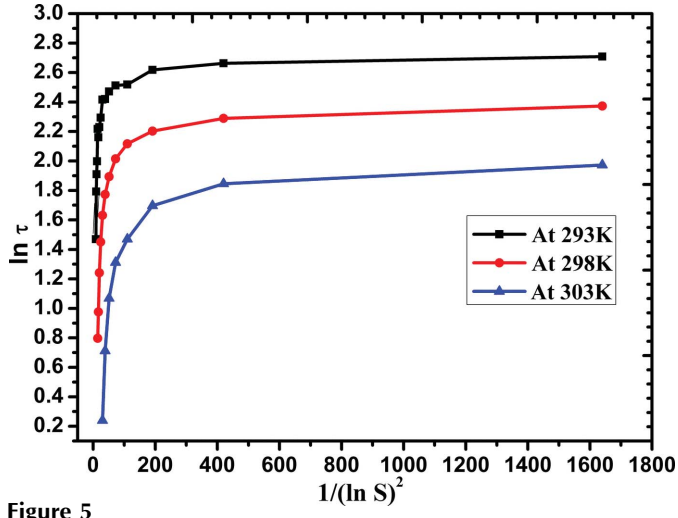

Figure 5
$\ln\tau$ *versus* $1/(\ln S)^2$ of L-LHBr.

Table 3
Experimental determination of interfacial energy for L-LHBr.

Saturation temperature (K)	Slope (m)	Intercept (B)	Interfacial energy (in mJ m^{-2})	
			Experimental	Theoretical
293	0.0042	2.2088	0.65	1.32
298	0.0178	1.5987	1.07	1.35
303	0.0269	1.0794	1.24	1.67

intercept and corresponding interfacial energy thus obtained. The theoretically calculated value of σ is also given in the table. Though there is a discrepancy between the theoretical and experimental values, the discrepancy is much less than what is seen when we compare the reported literature for similar compounds (Kanagasekaran *et al.*, 2007; Rajendran *et al.*, 2003). The interfacial energy values reported for organic molecules such as paracetamol lie in the range of 1.4–2.8 mJ m^{-2} and are around 1.4–1.8 mJ m^{-2} for ketoprofen. The interfacial energy values reported for semi-organic compounds lie in the range of 1.5–1.74 mJ m^{-2} for L-lutamic HCl (Selvaraju *et al.*, 2006), 2.7–3.2 mJ m^{-2} for L-histidine tetrafluoroborate (Rajendran *et al.*, 2003) and about 1.67–3.65 mJ m^{-2} for L-proline cadmium chloride monohydrate (Kandasamy *et al.*, 2008). Hence, the σ values obtained experimentally and theoretically, despite being not very closely associated with each other, are reasonably close when compared with the values mentioned above for other compounds.

Fig. 6 shows the variation of critical nuclei at different supersaturation ratios. The calculated radius of the critical nucleus varied between 19.93 and 3.39 nm as the supersaturation was increased from 1.1 to 1.4, and this nature is clearly shown in the graph. It can be asserted that as the supersaturation is increased the size of the critical nuclei decreases.

The response of the critical nucleation energy with varying supersaturation is shown in Fig. 7. This graph clearly shows that as the supersaturation is increased the barrier to the nucleation considerably decreases, favouring the nucleation mechanism.

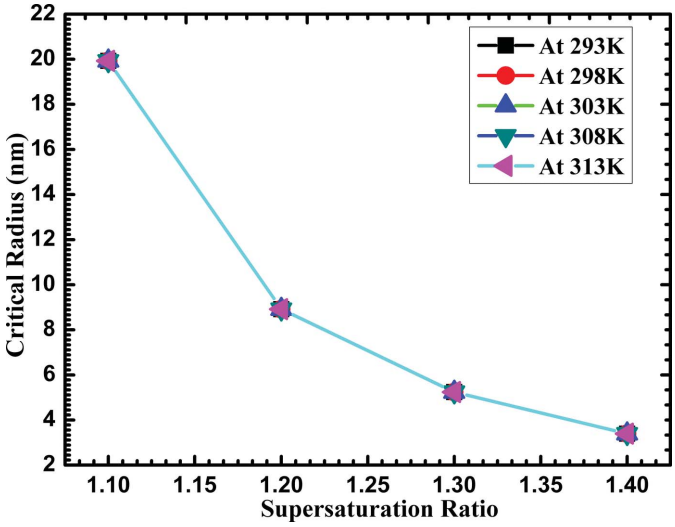

Figure 6
Critical radius *versus* supersaturation ratio of L-LHBr.

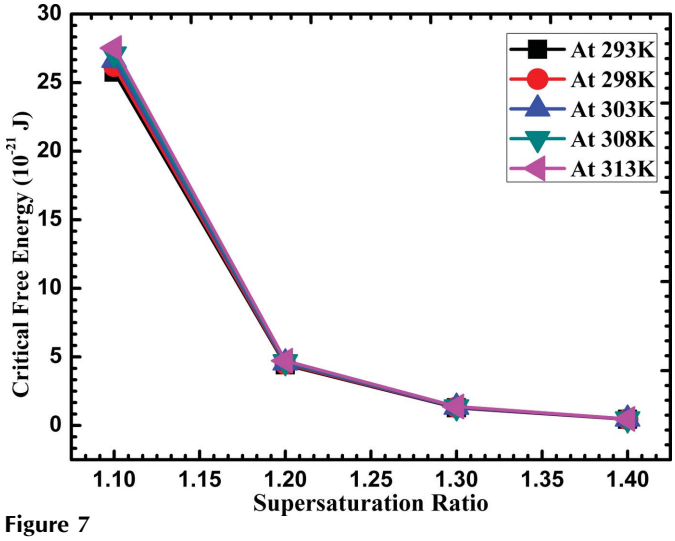

Figure 7
Critical free energy *versus* supersaturation ratio of L-LHBr.

3.2. Powder X-ray diffraction

A grown crystal was uniformly crushed into a fine powder to maintain the homogeneity. Powder X ray diffraction data were recorded using a Bruker D8 Advance powder X-ray diffractometer with Cu $K\alpha$ radiation of wavelength 1.54012 Å at a scan speed of 0.1° min^{-1} over the angular range 10–80°, in order to understand the crystal structure. The obtained spectrum (diffracted intensity *versus* twice the diffracting angle) with *hkl* indexed pattern showing the planes is presented in Fig. 8. The observed peaks are very sharp, indicating good crystallinity of the grown crystal. The recorded data were analysed using the *Check Cell* software (Krishna *et al.*, 2014) and the lattice parameters were calculated as a = 7.3072, b =

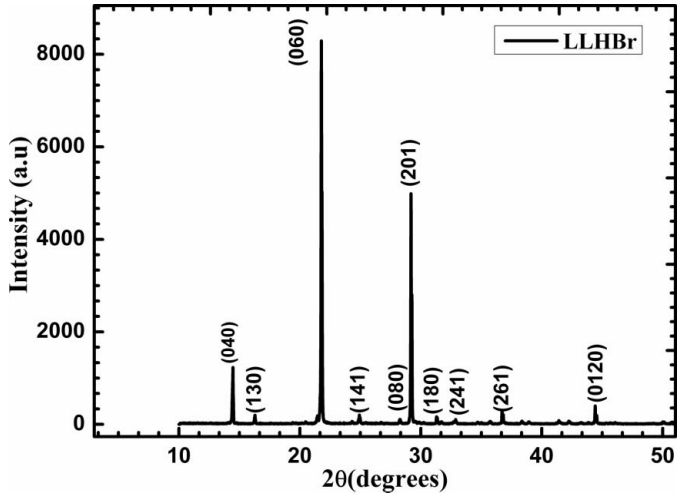

Figure 8
Powder XRD spectrum of L-LHBr.

24.4721, c = 5.5119 Å, $\alpha = \beta = \gamma = 90°$, confirming the orthorhombic structure. The lattice parameters are in very close proximity to the earlier reported values (Adhikari & Kar, 2013; Subramanian, 1967).

3.3. Raman analysis

The confirmation of functional groups present in the synthesized material was done through FT–Raman analysis using a Renishaw inVia Raman microscope. L-LHBr crystallizes in an orthorhombic ($P2_12_12_1$) space group. In the irreducible representations (IRep) of the C_2 factor group, the normal modes are decomposed as Γ = 132A + 132B, and as there are two acoustic modes at the B IRep and one at the A IRep, the optical modes are Γop = 131A + 130B. Fig. 9 presents the Raman spectrum of L-LHBr crystals in the spectral region 400–3100 cm^{-1}. The band at 444 cm^{-1} is assigned as skeletal structure deformations, δ(skel), while the intense band at 533 cm^{-1} is associated with the rocking of the (CO_2^-) unit, $r(CO_2^-)$. The band at 836 cm^{-1} represents an inversion of intensity for two scattering geometries; they are assigned as out-of-plane vibration of (CO_2^-) and $\gamma(CO_2^-)$. The vibrational peaks in the region 900–1100 cm^{-1} are associated mainly with several CC and CN stretching vibrations, ν(CC) and ν(CN). The band observed at 1138 cm^{-1} is assigned as the rocking of the NH_3^+ unit, $r(NH_3^+)$. The band at 1244 cm^{-1} is tentatively assigned as a torsion of CH_2, $\tau(CH_2)$. Most of the bands in the region 1300–1375 cm^{-1} are assigned as deformations of the CH unit, δ(CH), while the peaks at 1458 and 1478 cm^{-1} are associated with asymmetric bending of CH_3, $\delta a(CH_3)$. The bands observed at 1564 and 1585 cm^{-1} are associated with stretching vibrations of (CO_2^-) and $\nu(CO_2^{-1})$. Bands due to the stretching vibrations of methylene, methine and ammonium groups are expected to be observed in this high wavenumber region.

3.4. High-resolution X-ray diffraction

A PANalytical X'Pert PRO MRD high-resolution XRD system, with Cu $K\alpha_1$ radiation, was employed to assess the crystalline perfection of the grown crystals. The rocking curves of the crystals for the diffraction planes were recorded in symmetrical Bragg geometry using the natural facets by performing an ω scan (Bhagavannarayana & Kushwaha, 2010; Bhagavannarayana, Rajesh & Ramasamy, 2010) with double-axis geometry. The monochromated X-ray beam incident on the specimen was obtained using a high-resolution four-bounce Ge(220) monochromator. The diffracted beam from the specimen was detected by means of a scintillation detector without using any analyser at the receiving stage (*i.e.* before the detector), in order to allow the collection of all the possible information from the specimen crystal, such as the individual peaks from structural grain boundaries and scattered intensity from dislocations and other defects.

Fig. 10 shows the high-resolution X-ray diffraction curve (DC) recorded for a typical L-LHBr specimen crystal using (040) diffracting planes in symmetrical Bragg geometry by employing the MRD X-ray diffractometer described above with Cu $K\alpha_1$ radiation. As seen in the figure, the curve does not exhibit one single diffraction peak. The solid line, which follows the experimental points (filled circles) well, is the convoluted curve of two peaks using a Lorentzian fit. The additional peak is caused by the structural grain boundary. According to our earlier convention (Bhagavannarayana *et al.*, 2005), depending upon the tilt angle, *i.e.* the misorientation angle (α), of the boundary with respect to the two adjacent crystalline regions on either side of the boundary, the structural boundaries may be named as grain boundaries when $\alpha \geq 1°$, sub-grain or low-angle boundaries when $\alpha > 1'$ but less than a degree, and very low angle boundaries when $\alpha \leq 1'$. The tilt angle of the observed structural grain boundary is 12″ and hence the observed boundaries fall under the category of very low angle boundary. The FWHMs of the peaks corresponding to the main crystal block and the boundary are 40 and 10″. The relatively low FWHM values, which are very common for real life crystals (Senthil Kumar *et al.*, 2011), reveal that, though

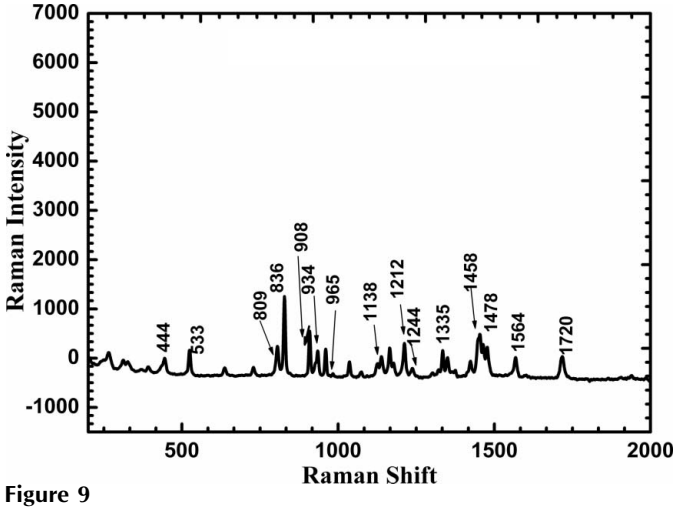

Figure 9
Raman spectrum of L-LHBr.

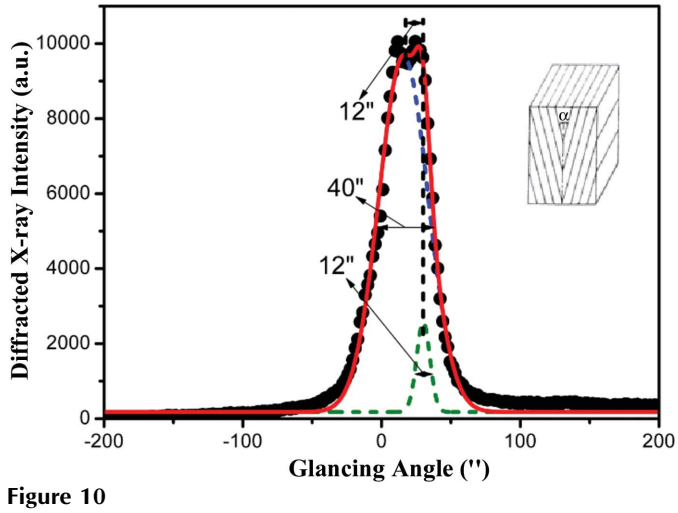

Figure 10
Diffraction curve recorded for a typical L-LHBr single crystal for the (040) diffracting planes by employing a PANalytical MRD diffractometer with Cu $K\alpha_1$ radiation. The inset shows a schematic of a structural grain boundary.

the crystal contains very low angle boundaries, the crystalline quality is quite good. The very low angle boundaries might have formed during the growth process as a result of entrapment of solvent molecules or impurities. These might have entered into the crystalline matrix initially as point defects, but later agglomerated as defect clusters and finally generated grain boundaries because of self-generated strains (Bhagavannarayana & Kushwaha, 2010; Bhagavannarayana, Rajesh & Ramasamy, 2010). It should be mentioned here that such low-angle boundaries could be detected with well resolved peaks in the diffraction curve only because of the high resolution of the diffractometer with its four-bounce monochromator. Such defects may not have much influence on the NLO properties. However, a quantitative analysis of such unavoidable defects is of great importance, particularly in the case of phase matching applications, as described in our recent article (Bhagavannarayana *et al.*, 2011).

3.5. Photoluminescence and time-resolved photoluminescence studies

A PL study can provide information about the different energy states between the valence band and conduction band of the crystal, marking the presence of f-centres/vacancies and other associated defects (Thukral *et al.*, 2014). Room-temperature steady-state PL excitation and PL emission of the L-LHBr single crystal were studied in the range 200–700 nm using a luminescence spectrometer (Make: Edinburgh; Model: F900) equipped with a xenon lamp and monochromators. For all the measurements, the slit width was constantly maintained at 19.90 nm. The lifetime measurements were recorded using the same instrument with a microsecond xenon flash lamp operating at a frequency of 40 Hz as the source of excitation.

3.5.1. Photoluminescence. Fig. 11 shows the PL emission spectrum obtained at an excitation of ~306 nm, revealing emission at ~461 nm. The broad band observed at ~405 nm is believed to be the transition caused by the presence of defects in the crystals, whereas the sharp peak at ~461 nm is due to the intrinsic optical behaviour of the L-LHBr crystal itself. All the results are in agreement with those obtained through HRXRD and etching studies.

3.5.2. Time-resolved photoluminescence. TRPL is a powerful tool used for the optical characterization of semi-organic single crystals. It is an eminent nondestructive technique to check the optical characterization of crystals with emphasis on the excitation dynamics (Vijayan *et al.*, 2014). Moreover, it highlights the crystalline quality of the single crystal, allowing us to design optimal device performance by calculating the excitation lifetimes. Fig. 12 shows the TRPL decay in the microsecond range (0–50 µs) for an excitation wavelength of 306 nm and an emission wavelength of 461 nm. Basically, it is a multiexponential process with a combination of various short and long decay processes. The longer the process, the deeper is the trap level. The data were fitted in analogy to an exponential decay pattern, and the deviation obtained is fairly low ($\chi^2 = 1.67$), suggesting an appropriate fit. The exponential behaviour of this decay pattern is mathematically expressed as

$$R(t) = A_1 \exp(-t/\tau_1) + A_2 \exp(-t/\tau_2) + A_3 \exp(-t/\tau_3). \quad (10)$$

Here τ_1, τ_2 and τ_3 are the decay constants. The constants A_1, A_2 and A_3 show the contributions of the respective decay components. The values of the decay components obtained from the fitted curve are $\tau_1 = 3.67$ µs, $\tau_2 = 1.80$ µs and $\tau_3 = 6.60$ µs. Thereby, we can deduce their nature as shallow and deep defects (Khan *et al.*, 2008; Thukral *et al.*, 2014; Vijayan *et al.*, 2014). The residuals shown in the inset of Fig. 12 indicate the quality of the fit to the actual TRPL decay curve.

3.6. Etching study

The study of etch pits is a well known technique to investigate the surface morphology of a crystal. The observed etch pits give details of the structural defects present in the crystal and the growth pattern in the crystal. Etching analysis was

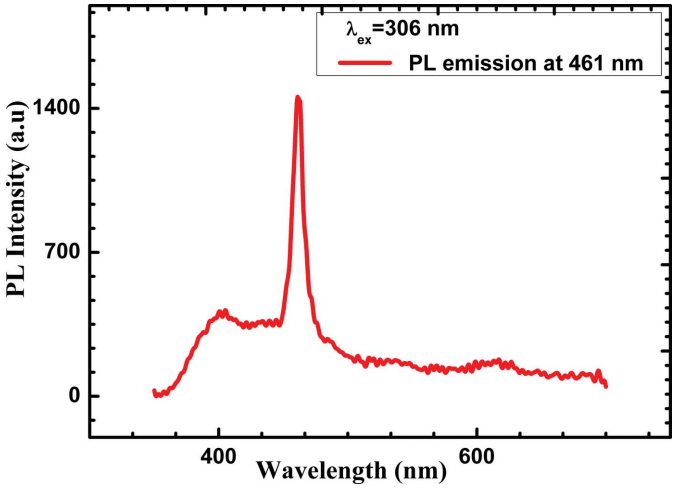

Figure 11
Photoluminescence spectrum for an L-LHBr crystal.

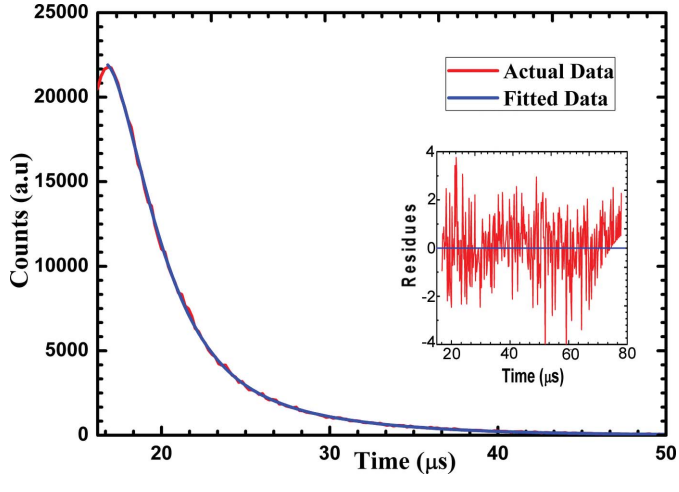

Figure 12
Time-resolved photoluminescence and residual for an L-LHBr crystal.

conducted using an optical microscope (model: Omni Tech) at a magnification of 100× at room temperature.

Growth of L-LHBr crystals depends on the pH of the mother solution. In general water, ethanol, methanol *etc*. are used as etchant because of their fast etching actions. The selection of etchant for an L-LHBr crystal is of marked importance as the surface of these crystals shows fogginess on dipping in water and other solutions with different pH from that of the solution in which the crystal was grown. As per the reported literature (Adhikari & Kar, 2013), a mother solution with a pH of 0.88 was selected as an appropriate etchant. The etched patterns so obtained are shown in Fig. 13. The pattern obtained for an as-grown crystal (Fig. 13*a*) shows the growth pattern for layered growth, which reveals the two-dimensional nucleation mechanism (Sun *et al.*, 2010). After dissolving the crystal for a duration of 10 s (Fig. 13*b*), the layered structure was still visible, along with the formation of hillocks, inferring the different dissolution rates of the layers of the crystal. The formation of hillocks is attributed to a fast nucleation rate (Krishna *et al.*, 2014). Etch pits, though not very remarkable, also appeared at the adjoining portions of the hillocks. This clearly shows that the rate of dissolution of the surface with dislocations through nucleation of pits along the dislocation line is greater than the rate of dissolution of the defect-free surface. Our observations strengthen the idea that these hillocks are basically composed of spirals, which occur because of dislocations in close association with each other (Mukerji & Kar, 1999).

After etching for 20 s duration (Fig. 13*c*), prominent screw-shaped etch pits are visible, with a considerable increase in the size of the etch pits. These distinct etch pits could also arise because of the high saturation of the etchant.

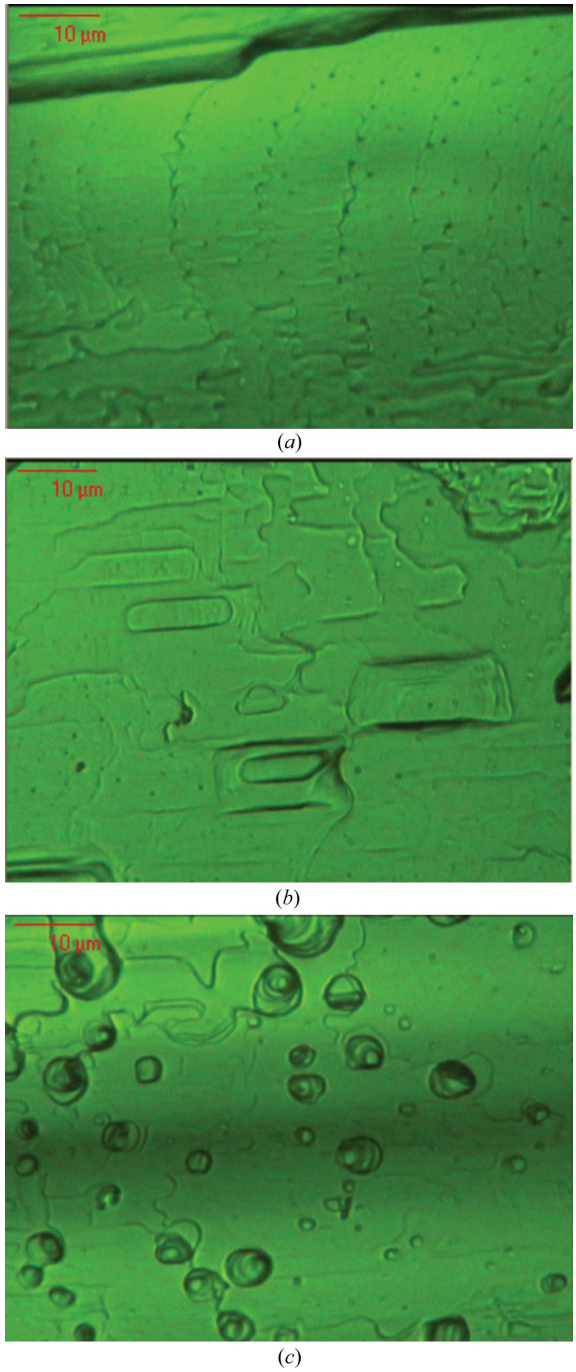

(*a*)

(*b*)

(*c*)

Figure 13
Micrographs of the surface of an L-LHBr crystal: (*a*) the as-grown crystal, (*b*) after etching for 10 s and (*c*) after etching for 20 s.

3.7. Third-order nonlinear optical properties

In order to explore the third-order nonlinear optical properties, *Z*-scan measurements have been performed by means of the open-aperture *Z*-scan technique (Sheik-bahae *et al.*, 1989; Subashini *et al.*, 2013). The fundamental unit for this characterization comprises an Nd:YAG (yttrium aluminium garnet) laser (Minilite I, Continuum), emitting 5 ns laser pulses at the second harmonic wavelength of 532 nm, associated with a converging lens (plano convex lens, $f = 100$ mm) to focus the beam and a laser detector for recording the output. The output laser beam is further passed through a spatial filter to obtain a clean Gaussian beam. The specimen is kept on a linear translation stage (Newport, ILS150PP), for moving to the required position about the beam focus, whose transmission direction is taken about the *Z* axis. The incident and transmitted pulse energies are recorded using pyroelectric probes (Laser Probe, RjP-735) at each position. The setup is also enabled with the *Lab View* program (Philip *et al.*, 2012) to coordinate the laser firing, movement of the stage and data recording.

The sample for this measurement was prepared by dispersing the material in double-distilled water. The average energy of the incident pulse lies in the region of 13.96 mJ. Fig. 14 shows the normalized transmission ($T_{\rm norm}$) obtained by translating the sample along the **Z** direction. As evident from the figure, the valley-shaped curve shows a maximum decrease in transmission about the focus $Z = 0$. This phenomenon is referred to as reverse saturation absorption, indicating nonlinear absorption (Rani *et al.*, 2013). The experimentally recorded *Z*-scan curve (represented by bubble symbols) is fitted using standard nonlinear transmission equations (shown as a solid line) to obtain the optical nonlinearity coefficient. The inset in the figure shows the normalized transmission

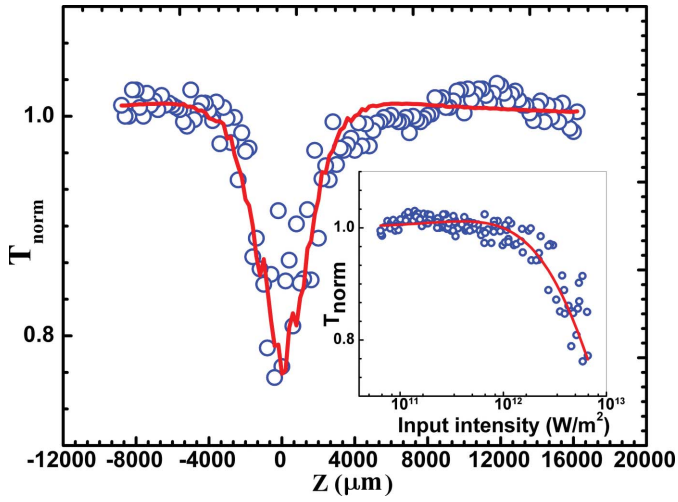

Figure 14
Open-aperture *Z*-scan measurements of an L-LHBr crystal.

versus the input intensity. Two-photon absorption is the basic mechanism responsible for this nonlinear transmission, and the two-photon absorption coefficient of L-LHBr is calculated to be 70×10^{-12} m W^{-1} in the present investigation.

4. Conclusions

In the present investigation, good quality L-LHBr single crystals were grown successfully in accordance with the growth parameters optimized through nucleation studies. Important parameters like induction period, metastable zone width, Gibbs free energy and interfacial energy have been determined. The studies revealed that good quality crystals can be grown at lower temperatures through the temperature lowering technique with a slow cooling rate. The L-LHBr crystals were subjected to XRD and Raman analysis for confirmation of the lattice parameters and identification of functional groups. Crystalline quality is a stringent parameter for device fabrication, and therefore its assessment was done through the technique of high-resolution X-ray diffraction analysis. It was found that the quality of the grown crystals is quite good. Furthermore, the nature of defects present in the crystals was analysed through time-resolved photoluminescence, and the surface of a crystal was reviewed through an etching study. The third-order nonlinear coefficient has also been determined through the widely used *Z*-scan method.

The authors are highly grateful to Professor R. C. Budhani, Director, CSIR–National Physical Laboratory, for encouragement and support for crystal growth activity. RR is thankful for financial assistance in terms of an INSPIRE scholarship granted by DST, Government of India.

References

Adhikari, S. & Kar, T. (2013). *Mater. Res. Bull.* **48**, 1612–1617.
Bhagavannarayana, G., Ananthamurthy, R. V., Budakoti, G. C., Kumar, B. & Bartwal, K. S. (2005). *J. Appl. Cryst.* **38**, 768–771.
Bhagavannarayana, G. & Kushwaha, S. K. (2010). *J. Appl. Cryst.* **43**, 154–162.
Bhagavannarayana, G., Rajesh, P. & Ramasamy, P. (2010). *J. Appl. Cryst.* **43**, 1372–1376.
Bhagavannarayana, G., Riscob, B. & Shakir, M. (2011). *Mater. Chem. Phys.* **126**, 20–23.
Kanagasekaran, T., Mythili, P., Srinivasan, P., Vijayan, N., Gopalakrishnan, R. & Ramasamy, P. (2007). *Cryst. Res. Technol.* **42**, 995–1001.
Kandasamy, A., Mohan, R., Lydia Caroline, M. & Vasudevan, S. (2008). *Cryst. Res. Technol.* **43**, 186–192.
Khan, A. F., Haranath, D., Yadav, R., Singh, S., Chawla, S. & Dutta, V. (2008). *Appl. Phys. Lett.* **93**, 073103–073105.
Krishna, A., Vijayan, N., Riscob, B., Gour, B. S., Haranath, D., Philip, J., Verma, S., Jayalakshmy, M. S., Bhagavannarayana, G. & Halder, S. K. (2014). *Appl. Phys. A*, **114**, 1257–1265.
Mukerji, S. & Kar, T. (1999). *J. Cryst. Growth*, **204**, 341–347.
Nielsen, A. E. (1964). *Kinetics of Precipitation.* Oxford: Pergamon Press.
Philip, R., Chantharasupawong, P., Qian, H., Jin, R. & Thomas, J. (2012). *Nano Lett.* **12**, 4661–4667.
Rajendran, K. V., Rajasekaran, R., Jayaraman, D., Jayavel, R. & Ramasamy, P. (2003). *Mater. Chem. Phys.* **81**, 50–55.
Rani, N., Vijayan, N., Riscob, B., Karan Jat, S., Krishna, A., Das, S., Bhagavannarayana, G., Rathi, B. & Wahab, M. A. (2013). *CrystEngComm*, **15**, 2127–2132.
Selvaraju, K., Valluvan, R. & Kumararaman, S. (2006). *Mater. Lett.* **60**, 1565–1569.
Senthil Kumar, K., Moorthy Babu, S. & Bhagavannarayana, G. (2011). *J. Appl. Cryst.* **44**, 313–318.
Senthil Pandian, M., Ramasamy, P. & Kumar, B. (2012). *Mater. Res. Bull.* **47**, 1587–1597.
Sheik-bahae, M., Said, A. A. & Van Stryland, E. W. (1989). *Opt. Lett.* **14**, 955–957.
Shkir, M., Ganesh, V., Vijayan, N., Riscob, B., Kumar, A., Rana, D. K., Shoeb Khan, M., Hasmuddin, M., Wahab, M. A., Ramesh Babu, R. & Bhagavannarayana, G. (2013). *Spectrochim. Acta A Mol. Biomol. Spectrosc.* **103**, 199–204.
Subashini, A., Bhagavannarayana, G. & Ramamurthi, K. (2013). *Spectrochim. Acta A Mol. Biomol. Spectrosc.* **104**, 403–408.
Subramanian, E. (1967). *Acta Cryst.* **22**, 910–917.
Sun, G. H., Zhang, G. H., Wang, X. Q., Sun, Z. H. & Xu, D. (2010). *Mater. Chem. Phys.* **122**, 524–527.
Teychené, S. & Biscans, B. (2008). *Cryst. Growth Des.* **8**, 1133–1139.
Thukral, K., Vijayan, N., Rathi, B., Bhagavannaryana, G., Verma, S., Philip, J., Krishna, A., Jeyalakshmy, M. S. & Halder, S. K. (2014). *CrystEngComm*, **16**, 2802.
Vijayan, N., Philip, J., Haranath, D., Rathi, B., Bhagavannarayana, G., Halder, S. K., Roy, N., Jayalakshmy, M. S. & Verma, S. (2014). *Spectrochim. Acta A Mol. Biomol. Spectrosc.* **122**, 309–314.
Yang, W., Lei, Z., Hu, Y., Chen, X. & Fu, S. (2010). *Ind. Eng. Chem. Res.* **49**, 11170–11175.